

# MONITORING SURFACE STATE OF AA7075-T6 DURING DYNAMIC LOADING WITH FBG SENSOR

Milkovic, M.\*; Njegovec, M.\*\*; Predan, J.\*; Javornik, J.\*\*; Djonlagic, D.\*\* & Gubelj, N.\*.#

\*Faculty of Mechanical Engineering, University of Maribor, Smetanova 17, 2000 Maribor, Slovenia

\*\*Faculty of Electrical Engineering, University of Maribor, Koroska 46, 2000 Maribor, Slovenia

E-Mail: marijana.milkovic303@gmail.com, matej.njegovec@um.si, jozef.predan@um.si, jure.javornik@um.si, denis.donlagic@um.si, nenad.gubelj@um.si (# Corresponding author)

## Abstract

The AA7075-T6 material is widely used in aerospace applications due to its favourable strength-to-weight ratio and cost-effectiveness. The material undergoes a process of cold rolling and subsequent stretching to form metal sheets. This process generates residual compressive stresses on the surface of the material. Surface changes in the material are observed at low stress levels, resulting in variations in residual stresses and surface roughness. This article presents an approach to monitor the surface state changes of AA7075-T6 material during dynamic loading using Fiber Bragg Grating (FBG) sensor. Numerical Finite Element Method (FEM) simulations analyse the transfer of deformations from the damaged surface through the adhesive layer to FBG with different cladding thicknesses. Loading induces microcrack-related intensity changes in the FBG optical spectrum and deformation response. The magnitude of the response is greater, when the cladding thickness of the optical fibre is thinner. Experimental results show that the FBG optical spectrum response varies with cumulative number of dynamic cycles.

(Received in June 2023, accepted in July 2023. This paper was with the authors 1 month for 3 revisions.)

**Key Words:** AA7075-T6, Dynamic Loading, Fiber Bragg Grating (FBG) Sensor, Surface Condition

## 1. INTRODUCTION

### 1.1 General

The goal of Structural Health Monitoring (SHM) of dynamically loaded components is to ensure reliable service of structure during lifetime. Uniaxial high-cycle fatigue tests have shown that many materials have a fatigue limit that guarantees infinite fatigue life under certain loadings [1]. Certain materials, like aluminium alloy, lack a fatigue limit and are more susceptible to fatigue fracture. It is important to ensure safe and reliable operation and recognize change of surface in early stage of loading. The goal is to detect and assess degradation processes that may occur on the surface of the material. Each component structure can be characterized by macroscopic quantities, such as stresses and strains, which are defined at each point of the body. To analyse the behaviour of the material, it is common to consider an elementary volume as the smallest representative sample that can be assumed to be homogeneous in its mechanical properties. At a mesoscopic scale, the material can be partitioned into regions that contain a large number of individual crystals. These crystals may have different orientations, sizes, and shapes, leading to variations in their mechanical properties. Previous research [2] demonstrated that fatigue induces local plasticization and separation processes near inclusions or grain boundaries, which are imperfections on the surface of the material. As a result, the mesoscopic stresses and strains within these regions are not uniform, as they can differ from one grain to another [1, 3-11]. These processes result in changes in surface roughness and the magnitude of residual stresses. Based on this understanding, the utilization of Fiber Bragg Grating (FBG) sensors was proposed to monitor the surface changes of dynamically loaded AA7075-T6 alloy. Fibre optic sensors, including distributed optical fibre sensors, have been widely employed for structural health monitoring

(SHM) of various structures [12, 13]. SHM aims to assess the condition and integrity of structures [14]. In the case of our study, we are specifically interested in monitoring the changes in surface conditions using FBG optical sensors.

FBG sensors and optical fibre sensors, in general, have a wide range of applications. They have been used for various purposes e.g., for emulsion concentration measurement [15], refractive index dispersion measurement [16], corrosion monitoring [17] and many others, e.g. [18]. In this investigation, we utilized the standard grating mode fibre with a linear grating period. The optical fibre, which is bonded to the surface with an adhesive layer, undergoes extensions along its length during tensile mechanical loading of the substrate material [19]. The main objective of our study is to assess the reliability of the established setup, which includes the metal substrate, adhesive layer, and optical fibre, for long term dynamic loading measurements. The focus is on analysing the response of the FBG optical sensor with different thickness of the cladding layer. Additionally, we aim to investigate whether there are changes in the surface strain response during high cycle dynamic loading. The paper will present numerical simulations to analyse the transfer of non-uniform strain from the surface of AA7075-T6 to the FBG sensor with different thicknesses of the cladding. Experimental measurements of the optical spectrum response using the FBG sensor will also be conducted. The combined numerical and experimental analysis will provide insights into the behaviour of the FBG under dynamic loading conditions and its potential for monitoring surface strain changes over extended periods of time.

## 1.2 Material

Aluminium alloys are commonly employed in the design of aerospace components due to their favourable combination of lightweight and high strength characteristics. However, it is important to note that aluminium alloys, unlike steels, do not possess a fatigue limit, making them more susceptible to fatigue fracture [20]. The mechanical properties of AA7075-T6 sheet are achieved through a combination of chemical composition and thermomechanical treatment. The chemical composition of the AA7075-T6 alloy is listed in Table I.

Table I: Chemical composition in weight % of AA7075-T6.

Al	Zn	Mg	Cu	Cr	Fe	Si	Ti	Mn	Ga	Zr
89.4	6.04	2.23	1.74	0.19	0.099	0.09	0.03	0.016	0.11	0.004

To evaluate the mechanical behaviour, tensile flat specimens were prepared by cutting them from the sheet plate, and subsequent testing was conducted following the DIN 50125 standard. The experimental results of mechanical properties are given in Table II. The microstructure of the AA7075-T6 alloy was examined using optical microscopy at magnification of  $\times 50$ , as shown in Fig. 1. The average crystal grain size of the alloy was determined to be  $31.3 \mu\text{m}$  in the longitudinal direction and  $29.6 \mu\text{m}$  in the transverse direction. Additionally, two types of inclusions were observed on the surface of the sample. The first type of inclusion consisted of Al, Mg, Fe, Cu, and Zn, and exhibited an elongated shape with non-equal diagonals. Fig. 2 illustrates the presence of these inclusions on the surface of the material. The average size of the inclusions at the two examined sites ranged between 6 to  $15 \mu\text{m}$ . For the adhesive fixation of FBG sensors, the surfaces of all specimens were uniformly polished using the same method.

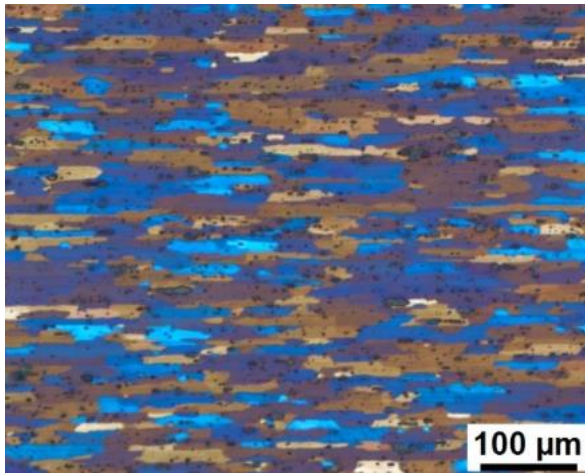
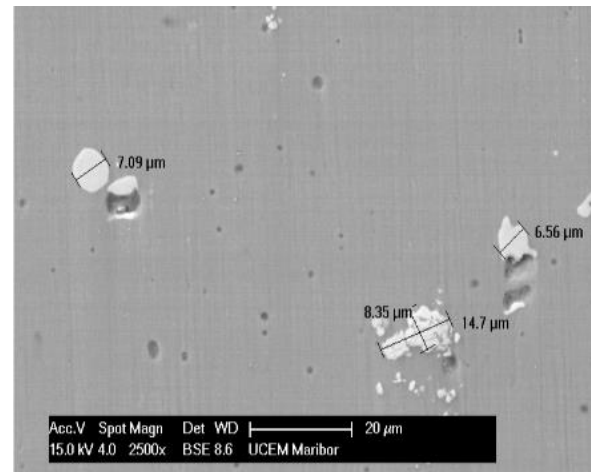


Figure 1: Sample 1 of cold rolled AA7075-T6.

Figure 2: Measured size of inclusions,  $\times 500$ .

## **2. NUMERICAL SIMULATION OF TENSILE LOADING OF SPECIMEN WITH FBG SENSOR**

To investigate the strain response of the FBG optical fibre, 2D numerical simulations were conducted using the ABAQUS explicit software. This suggests that the depth of the crack plays a crucial role in determining the magnitude and extent of stress concentration [21, 22].

The focus was on analyzing the influence of cladding thickness and grain size on the response spectrum of the FBG sensor. Multiple cracking surfaces with varying crack distances were designed to simulate different grain sizes. The simulation also considered the crack depth to assess the impact of increasing surface damage on the optical spectrum response during high-cycle loading. To accurately simulate the stress-strain behavior and strain transmission from the surface to the optical fibre core, the tensile mechanical properties of various material compositions were used. The properties specific to the AA7075-T6 material were obtained from both literature sources and the laboratory of optical sensors at the University in Maribor. The grain size and orientation information, as presented in Table II, was obtained through examination in a metallographic laboratory.

Table II: Tensile properties of materials for numerical simulations.

Material	Young Modulus [GPa]	Poisson ratio, $\nu$	Yield stress [MPa]	Tensile strength [MPa]	Elongation [%]
Al7075-T6	66.3	0.33	451	525	12
Epoxy 353ND	3.7	0.407	36	58.7	8.7
SMF-28 Optical Fibre Core	72.37	0.17	/	/	/
SMF-28 Optical Fibre Cladding	72.45	0.17	/	/	/

To ensure control over the FBG response process, a model was created with AA7075-T6 as the substrate. An optical fibre was attached to the substrate using an adhesive layer. The optical fibre consisted of a protective cladding layer and a core with reflective gratings. Fig. 3 provides a schematic representation of the model, with functional designations assigned to each geometric parameter. Table III presents typical parameter sizes that were varied during the numerical simulations, enabling a comprehensive system analysis.

This investigation focused on detecting changes on the surface of a dynamically loaded sample caused by short cracks that are smaller than the grain size in AA7075-T6. An optical fibre was used to detect these changes. The cracks on the surface were assumed to have a depth of  $e = 5 \mu\text{m}$ , which is several times smaller than the average grain size of  $30 \mu\text{m}$ . The aim was

to assess how the response of the FBG reflection spectrum changes as the cracks propagate between the grains. Numerical simulations were conducted to determine the stress-strain states and the corresponding changes in the FBG response for cracks with a depth of  $e = 20 \mu\text{m}$ . Different crack spacings on the surface:  $d = 30 \mu\text{m}$  and  $d = 120 \mu\text{m}$  were considered to account for the varying grain sizes in the material. The influence of the adhesive layer was also analysed by considering models with adhesive layer thicknesses of  $a = 1 \mu\text{m}$  and  $a = 5 \mu\text{m}$ . These simulations provided a comprehensive understanding of how crack depth, crack spacing, and adhesive layer thickness impact the FBG response.

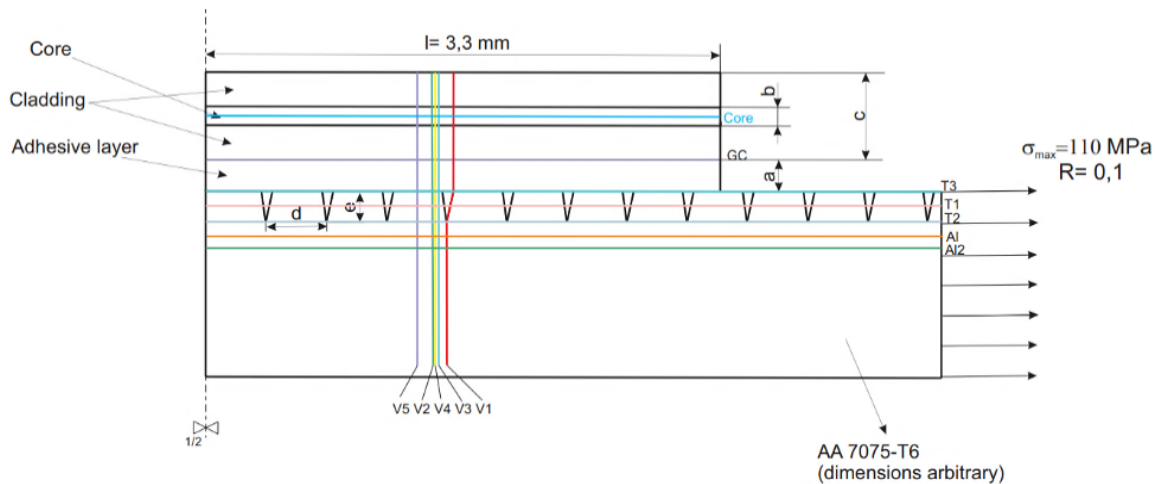


Figure 3: Schematic view of a bonded 2D model used for numerical analysis with path for results measurements in horizontal direction T1, T2, T3, Al, Al2 and vertical direction V1, ..., V5.

A total 16 different combinations of the 2D model were analysed in these simulations, as summarized in Table III. The numerical model incorporates variations in the thickness of the adhesive layer ( $a$ ), ranging from 1 to 5  $\mu\text{m}$ . The spacing between surface cracks ( $d$ ) was varied at values of 30  $\mu\text{m}$  and 120  $\mu\text{m}$ , corresponding to the grain size of the AA7075-T6 material. Two different depths of cracks ( $e$ ) were considered for the surface cracks, namely 5  $\mu\text{m}$  and 20  $\mu\text{m}$ . The protective layer of the FBG fibre was examined in two dimensions, with values of ( $c$ ) set at 40  $\mu\text{m}$  and 120  $\mu\text{m}$  for comparison. The diameter of the fibre core remained constant at 8.2  $\mu\text{m}$  throughout the simulations. A 2D numerical model was created with a structured mesh for analysis. The model had a fixed edge on the left side, and the AA7075-T6 base material was subjected to a tensile stress of  $\sigma_{\text{max}} = 110 \text{ MPa}$  on the right side. During the simulation, the metal substrate AA7075-T6 was stretched until it reached the maximum tensile stress at the right side of the model, while the left side was constrained. Fig. 4 illustrates the partitions that were created for each material separately, and the interconnection between these partitions was achieved using a structured mesh of finite elements. The left vertical edge of the specimen is set with symmetry boundary condition ( $U_1 = 0$ ), indicating no horizontal displacement. The bottom horizontal edge is set with a fixed displacement boundary condition ( $U_2 = 0$ ), indicating that it is fixed and cannot move. The right vertical edge is subjected to a tensile stress of 110 MPa, representing the applied pulling force. The mesh used was a quad and structured mesh. The global size of the FBG in FE model is 5 mm. The global size of the AA7075-T6 material FE model alone is 10 mm. The element type used in the analysis is plane stress, which is suitable for modelling 2D structures subjected to in-plane loading as is similar to ref. [23-29].

Fig. 5 represents the results of the numerical simulation of the model with an FBG sensor. The simulation includes a cladding thickness of 40  $\mu\text{m}$ , an adhesive bound layer thickness of 1  $\mu\text{m}$ , a distance of 30  $\mu\text{m}$  between multiple cracks, and two different crack depths: a) 5  $\mu\text{m}$  and b) 20  $\mu\text{m}$ . Fig. 5 illustrates distribution of von Mises stress for samples with varying crack

depths, illustrating upper limit of von Mises stress set to 130 MPa. Fig. 5 compares the specimens with the two different crack depths: a) 5  $\mu\text{m}$  and b) 20  $\mu\text{m}$ , in terms of von Mises stress. It shows the von Mises stress distribution in the Al7075-T6 material, highlighting the stress concentrations at the crack tips. It is observed that the crack tips exhibit stress concentrations, with higher von Mises stress values at the crack tip for longer cracks (b) 20  $\mu\text{m}$ ) compared to shorter cracks (a) 5  $\mu\text{m}$ ). Locally, it is observed that the von Mises stress values at the crack tips exceed the yield stress of the material, indicating the potential for stress concentrations and potential failure initiation at those locations. With a deeper crack (20  $\mu\text{m}$ ), the stress concentration is more prominent and extended over a larger area, indicating a higher level of stress concentration.

Table III: Selected 16 combinations for FEM analysis with different geometrical parameters of model.

Cladding diameter, [ $\mu\text{m}$ ]	<i>C</i>	40								125							
Adhesive layer thickness, [ $\mu\text{m}$ ]	<i>A</i>	1				5				1				5			
Grain size, [ $\mu\text{m}$ ]	<i>d</i>	30		120		30		120		30		120		30		120	
Cracks depth, [ $\mu\text{m}$ ]	<i>e</i>	5	20	5	20	5	20	5	20	5	20	5	20	5	20	5	20
Combination:		<b>1</b>	<b>2</b>	<b>3</b>	<b>4</b>	<b>5</b>	<b>6</b>	<b>7</b>	<b>8</b>	<b>9</b>	<b>10</b>	<b>11</b>	<b>12</b>	<b>13</b>	<b>14</b>	<b>15</b>	<b>16</b>

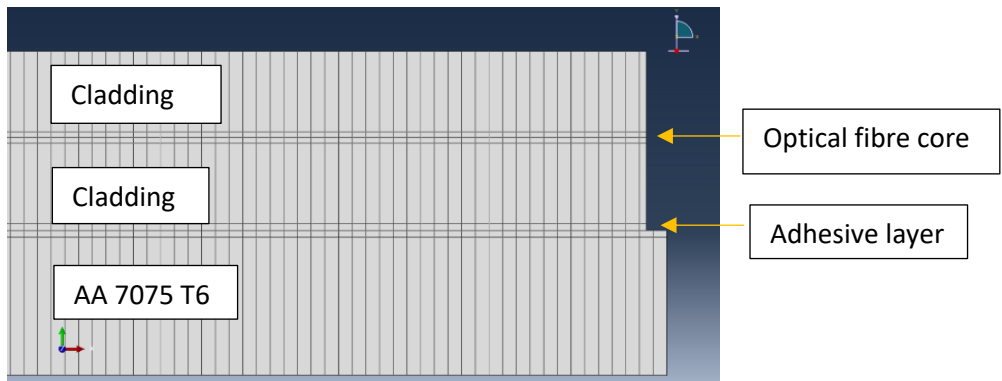
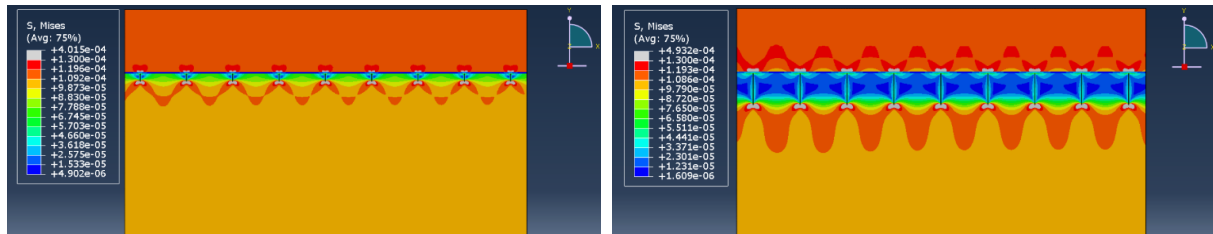


Figure 4: Meshing of the model in ABAQUS with partitions which present some material in loading system.

Sample ( $c=40$   $a=1$   $d=30$   $e=5$ ) 40\_1\_30\_5

Sample ( $c=40$   $a=1$   $d=30$   $e=20$ ) 40\_1\_30\_20



a) Substrate with 5  $\mu\text{m}$  short cracks exhibiting an upper limit of von Mises stress of 130 MPa

b) Substrate with 20  $\mu\text{m}$  long cracks exhibiting an upper limit of von Mises stress 130 MPa

Figure 5: Distribution of von Mises stress with different crack depth exposed to  $\sigma_{\text{max}} = 110$  MPa.

Fig. 6 illustrates the distribution of stress components  $\sigma_{11}$  in the loading directions for the same models as shown in Fig. 5, with crack depth 5  $\mu\text{m}$  and 20  $\mu\text{m}$ . By changing the upper limit of the  $\sigma_{11}$  value, a clearer visualization of stress concentration around the crack area can be observed. The stress is transmitted through the adhesive layer to the fibre cladding and

consequently to the core. The presence of a crack significantly affects the stress pattern. For a 5  $\mu\text{m}$  crack, the stress distribution near the crack is relatively more uniform, with slightly elevated stress levels compared to the surrounding region. However, with a 20  $\mu\text{m}$  crack, the stress concentration around the crack tip becomes more pronounced, resulting in higher stress values. This can be attributed to the larger crack size, which creates a more significant stress concentration effect. These observations highlight the importance of considering crack depth when assessing stress distributions in cracked materials. Deeper cracks lead to more pronounced stress concentrations, indicating a higher susceptibility to failure and potential fracture initiation. Fig. 7 presents the shear stress distributions at the crack tips for both numerical configurations, as described in Fig. 5. It is evident that the model with deeper cracks (b) 20  $\mu\text{m}$ ) exhibits more pronounced stress concentrations compared to the model with shallower cracks (a) 5  $\mu\text{m}$ ).

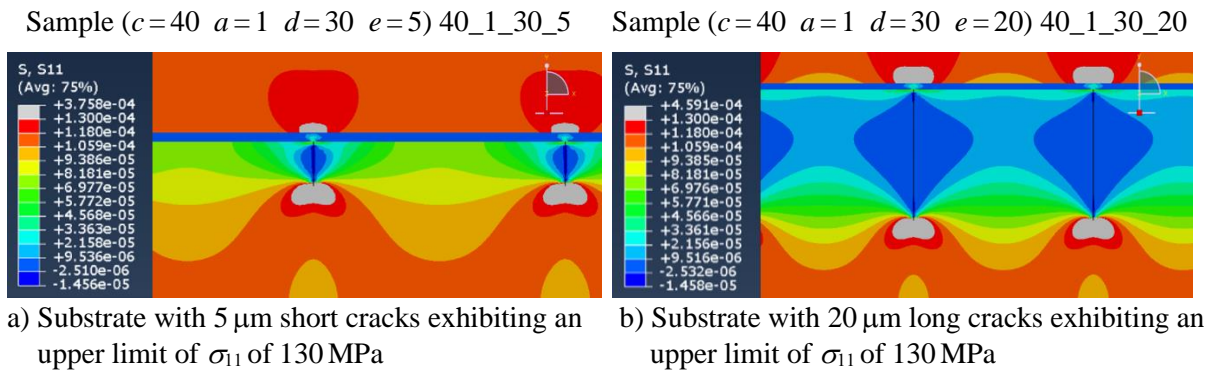


Figure 6: Distribution of normal stress  $\sigma_{11}$  for samples with different crack depth exposed to  $\sigma_{\text{max}} = 110$  MPa.

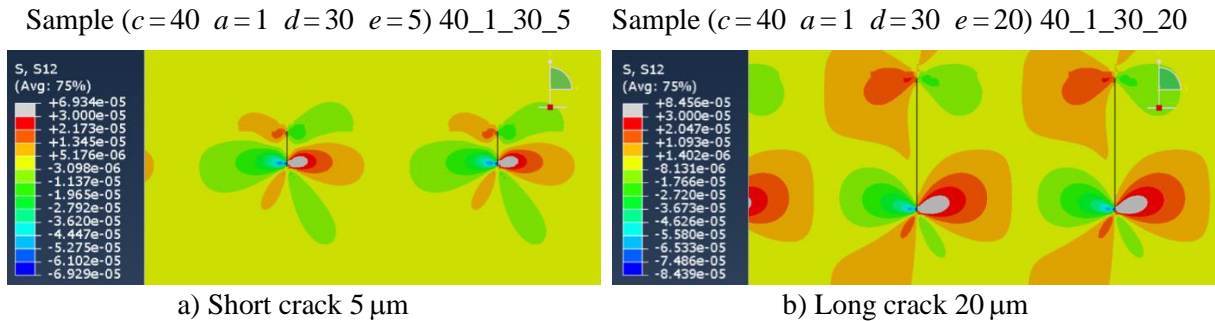


Figure 7: Shear stress  $\tau_{12}$  distribution for samples with different crack depth exposed to  $\sigma_{\text{max}} = 110$  MPa.

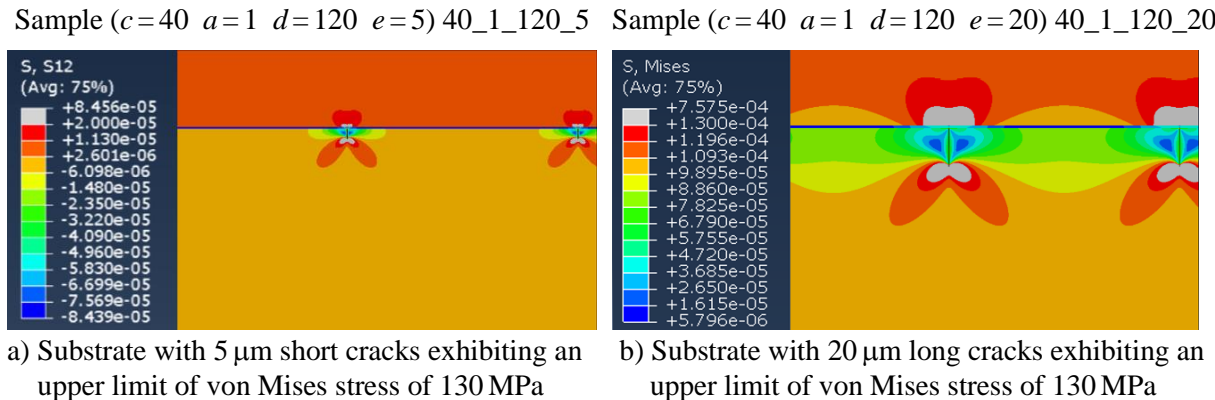


Figure 8: Von Mises stress distribution for samples with different crack depth and grain size of 120  $\mu\text{m}$  subjected to  $\sigma_{\text{max}} = 110$  MPa.

Fig. 8 presents the distribution of von Mises stress at tip of the crack when the grain size is 120  $\mu\text{m}$ . Comparing it with Fig. 5, it can be concluded that larger grain size can exhibit more significant plasticity compared to smaller grain size. It can also be observed that even with larger grain size, the transmission of strain through the adhesive layer and cladding of the optical fibre remains substantial. Similar conclusions can be drawn for stress in the loading direction ( $\sigma_{11}$ ) as depicted in Fig. 9.

The deformation reading lines in both the horizontal (AL, AL2, T1, T2 and T3) and vertical (V1, V2, V3, V4 and V5) directions are schematically represented in Fig. 3. The results are presented graphically along specific horizontal and vertical cross-section lines to visualize the values. Additionally, the deviations at characteristic points were separately illustrated to provide a more accurate representation of the deformation shape.

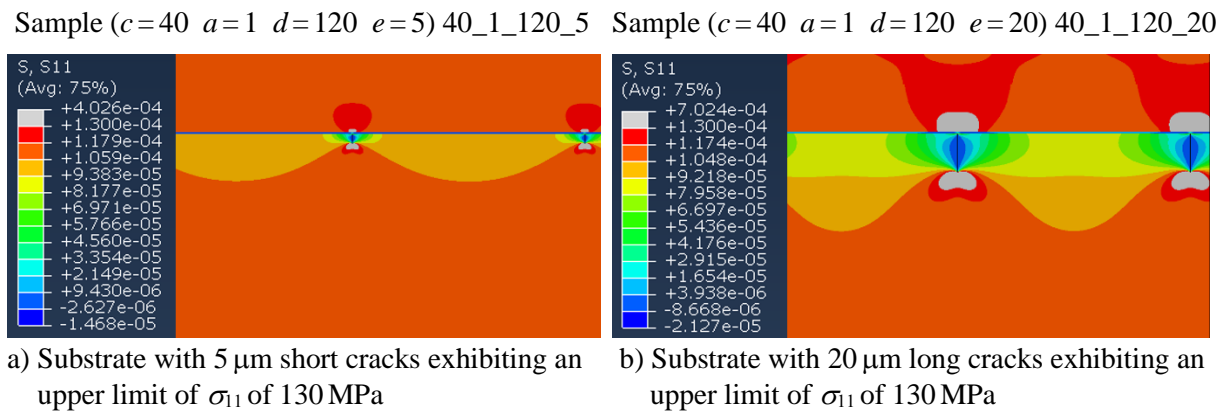


Figure 9: Normal stress  $\sigma_{11}$  distribution for samples with different crack depth and grain size of 120  $\mu\text{m}$  exposed to  $\sigma_{\text{max}} = 110$  MPa.

Fig. 10 illustrates the distribution of strain ( $e_{11}$ ) along the core of the FBG sensor for the 16 selected examples listed in Table III. It can be observed that the models with a thinner cladding layer ( $c = 40$   $\mu\text{m}$ ), thinner adhesive layer ( $a = 1$   $\mu\text{m}$ ), longer distance between cracks ( $d = 120$   $\mu\text{m}$ ), and deeper cracks ( $e = 20$   $\mu\text{m}$ ) exhibit higher periodic deviations in strain. The FBG core shows differences in strain ( $e_{11}$ ) for the thickest cladding layer ( $c = 120$   $\mu\text{m}$ ), thicker adhesive layer ( $a = 5$   $\mu\text{m}$ ), shorter distance between cracks ( $d = 30$   $\mu\text{m}$ ), and shallower cracks ( $e = 5$   $\mu\text{m}$ ). However, experimental testing is required to validate these findings.

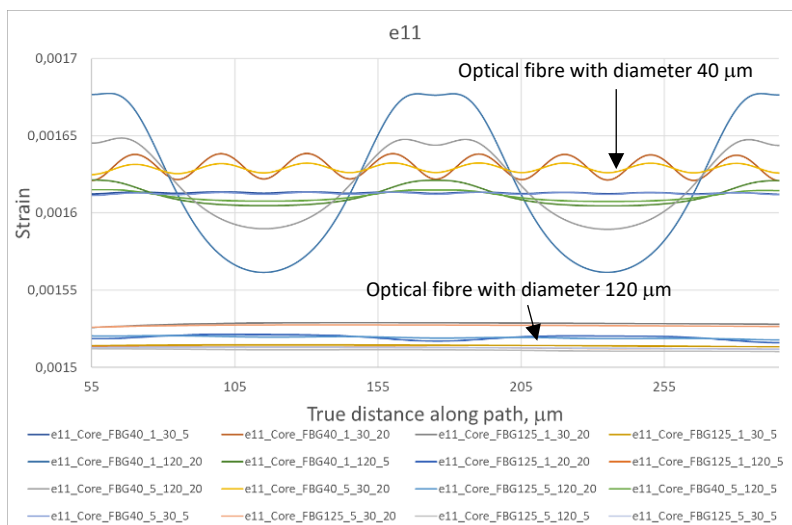


Figure 10: Strain  $e_{11}$  distribution along the core of FBG for all selected 16 examples.

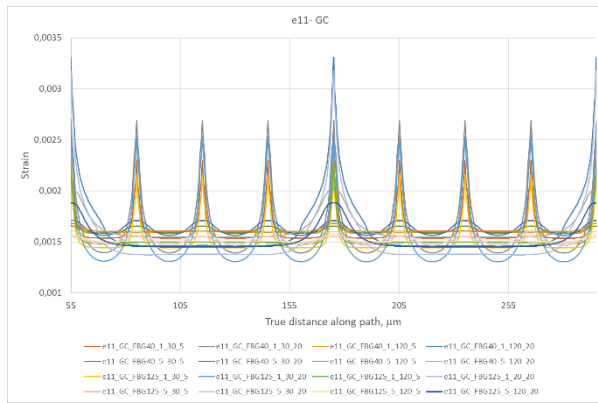


Figure 11: Horizontal strain  $e_{11}$  distribution along the border of adhesive layer and cladding of FBG for all selected 16 examples.

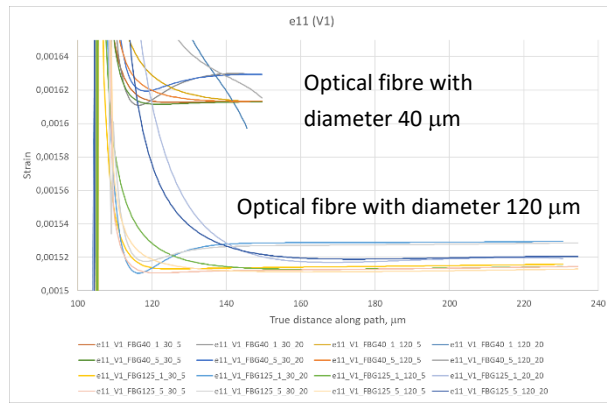


Figure 12: Strain  $e_{11}$  distribution for V1 section.

Fig. 11 illustrates the distribution of strain ( $e_{11}$ ) along the border of the adhesive layer and cladding of the FBG sensor for all 16 selected examples. In these simulations, the substrate material AA7075 T6 was subjected to a tensile stress of 110 MPa. The figure demonstrates that the thickness of the adhesive layer has a relatively minor impact on the strain  $e_{11}$  distribution compared to the thickness of the cladding layer.

Fig. 12 displays the strain  $e_{11}$  distribution along the crack in the V1 section (as shown in Fig. 3) for two different cladding thicknesses: 40  $\mu\text{m}$  and 120  $\mu\text{m}$ . The results indicate that the thinner cladding layer induces significantly higher strain compared to the thicker layer in all cases. Additionally, for the same crack depth, a larger grain size leads to higher strain in the optical core compared to a smaller grain size.

### **3. FATIGUE TESTING OF TENSILE SPECIMENS**

Preliminary fatigue tests were conducted on the samples using an INSTRON 1255 servo hydraulic testing machine. The samples have been subjected to uniaxial loading with a stress amplitude range of  $\Delta\sigma = 100$  MPa and a stress ratio of  $R = 0.1$  at room temperature.

#### **3.1 Fatigue testing of samples with FBG sensors**

FBG sensors were employed in the study using single-mode fibre SMF-28, inscribed with a femtosecond laser. The production process for the FBG sensors is detailed in [12]. The SMF length was trimmed to approximately 5 mm. Three FBG sensors with varying fibre diameters (125  $\mu\text{m}$ , 80  $\mu\text{m}$ , and 60  $\mu\text{m}$ ) were positioned on the polished surface of the specimen and securely attached using Epoxy 353 ND adhesive. A fourth sensor with a thickness of 125  $\mu\text{m}$  was attached perpendicularly to the first three sensors to compensate for temperature variations.

To monitor temperature variations and strain, all four sensors were connected to an FBG spectral interrogator, specifically the NI PXIe-4844. Fatigue testing of the specimens equipped with FBG sensors was conducted using tensile specimens of identical geometry. The cyclic loading amplitude was set at  $\Delta\sigma = 100$  MPa, and the loading ratio was maintained at  $R = 0.1$ . The tests were performed at room temperature, within the range of 23°C to 26°C. To capture the gradual changes occurring on the surface, measurements were conducted periodically at specific intervals. Initially, measurements were taken when the test specimen was free from any applied load. Subsequently, measurements were recorded after 30,000 cycles and then after 500,000 cycles, encompassing both the minimum and maximum dynamic stress loading conditions. Each sensor designed to measure tensile elongation yielded a distinct yet similar reflected optical spectrum. Each sensor, irrespective of its thickness, exhibits a distinct reflected

spectrum. This spectrum undergoes a shift in both mean wavelength and intensity of reflection in response to the applied load.

Fig. 13 a provides an example of the shift in the reflected frequency spectrum for an FBG with a thickness of 80  $\mu\text{m}$  after 30,000 and 500,000 cycles of loading at a constant stress and frequency of 12 Hz. On the other hand, Fig. 13 b displays the shift in the reflected frequency spectrum for an FBG with a thickness of 60  $\mu\text{m}$  after 30,000 and 500,000 cycles of loading at a constant voltage and frequency of 12 Hz. From the comparison between Figs. 13 a and 13 b, it is evident that when using an optical fibre thickness of 80  $\mu\text{m}$ , the difference in the position and height of the reflected spectrum is relatively small. However, with an optical fibre thickness of 60  $\mu\text{m}$ , the difference becomes more pronounced, particularly between 30,000 cycles and after 500,000 loading cycles. The change in the average wavelengths of the reflected spectrum for each FBG sensor can be determined based on the results shown in Figs. 13 a and 13 b. These figures demonstrate the shift in the position of the reflected spectrum under different loads for FBG sensors with different thicknesses. By analysing the data from these figures, it is possible to quantify the change in the average wavelengths of the reflected spectrum as a function of the applied load for each individual FBG sensor.

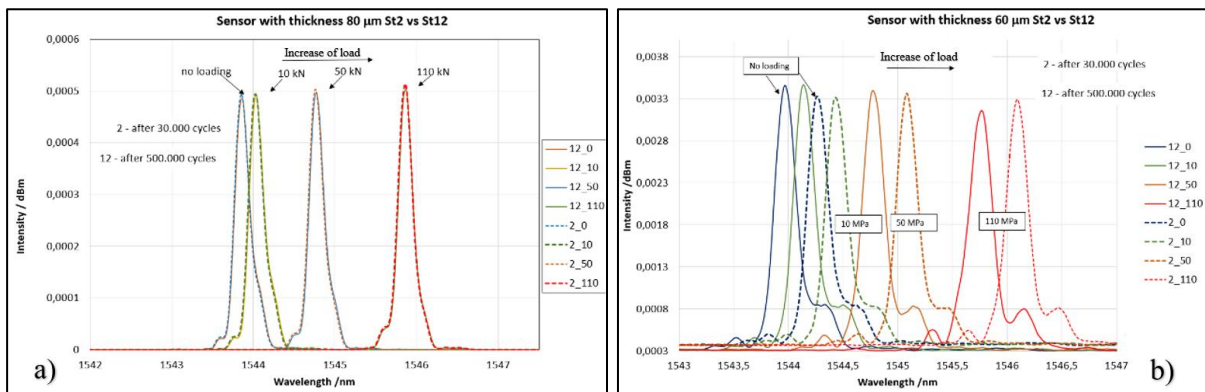


Figure 13: Comparison between optical response spectra after 30,000 cycles and 500,000 cycles for FBG with thickness: a) 80  $\mu\text{m}$ ; b) 60  $\mu\text{m}$ .

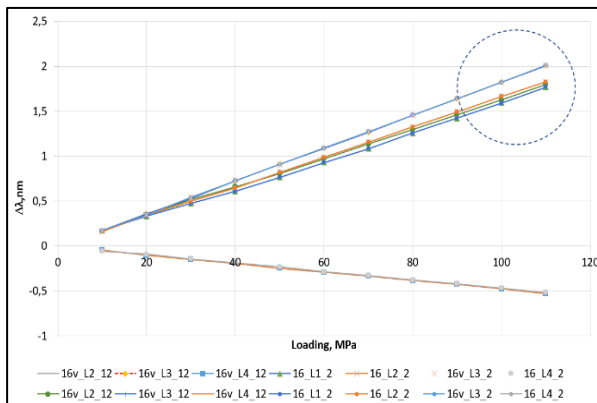


Figure 14: Change of wavelength  $\Delta\lambda$  with increasing of loading.

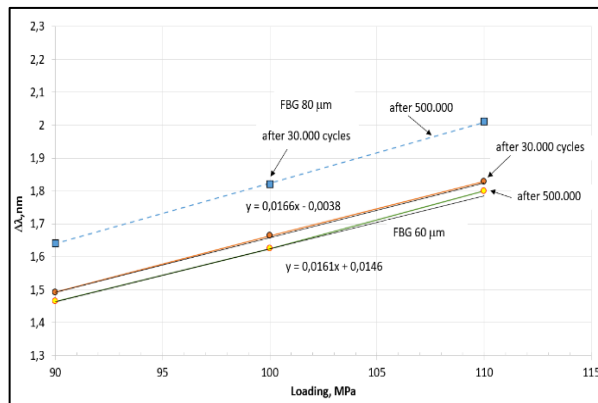


Figure 15: Detail from Fig. 14; change of wavelength  $\Delta\lambda$  only appear at FBG sensor with 60  $\mu\text{m}$  thickness.

Fig. 14 depicts the change in wavelength ( $\Delta\lambda$ ) with increasing load. Based on the observations in Fig. 14, it can be concluded that the change in the average values of the reflected spectrum exhibits a linearly increasing relationship with the applied load for the longitudinally placed FBG sensor. Fig. 15 illustrates detail view from Fig. 14, where it is evident that Fig. 15 shows that shift and slope change occurred only at FBG sensor with thickness of 60  $\mu\text{m}$ , while

the sensors with thickness of 80  $\mu\text{m}$  or thicker are too rigid to detect change of surface between different number of loading cycles. Experimental results indicate that the optical spectrum intensity and deformation response in the FBG fibre are significantly affected by the thickness of the optical fibre cladding. Thinner claddings result in a more pronounced change in the optical spectrum. The response of the optical spectrum in the FBG varies with the number of dynamic cycles, with a greater response observed in cases where the cladding thickness is smaller. Furthermore, experimental measurements of the optical fibre response before and after fatigue revealed a shift and redistribution of the frequency response among the samples. These findings suggest that the state of the surface, influenced by fatigue loading, impacts the behaviour of optical fibres and spectral response.

#### **4. CONCLUSION**

The article demonstrates the potential application of an FBG optical sensor for monitoring surface conditions, considering variations in cladding thickness and the number of cycles. The study includes numerical simulations and experimental testing to assess the performance of the sensors. Key findings from the numerical simulation include that the deeper cracks result in more significant stress concentration and higher stress levels. Larger grain sizes exhibit more significant plasticity and facilitate better transmission of strain. Models with thinner cladding layers, thinner adhesive layers, longer distances between cracks, and longer cracks exhibit higher periodic deviation in strain. The simulations also highlight the importance of cladding thickness in strain measurement sensitivity. Thicker cladding layers reduce the ability of optical sensor to accurately detect and measure strain. The experimental testing of FBG sensors with different cladding thicknesses confirms the simulation findings. Thinner cladding leads to a more sensitive response in detecting surface changes during dynamic loading. The linear relationship between the change in medium wavelength and applied stresses is maintained in sensors with thicker cladding, while thinner cladding sensors exhibit noticeable differences in the response. To effectively monitor the changes in the surface state during dynamic loading, it is advisable to use FBG sensors with thinner cladding that is appropriate for the grain size and mechanical properties of the substrate material. This ensures a higher sensibility to strain and enables accurate detection of surface changes.

Future research plans are aimed to discover effect of deeper crack length and larger grain size influence on strain response of FBG sensor.

#### **ACKNOWLEDGEMENT**

The authors acknowledge the Slovenian Research Agency ARRS for funding the Core Research Program P2-0137 "Numerical and experimental analysis of nonlinear mechanical systems" and funding Ph.D. study of Ms Marijana Milković.

#### **REFERENCES**

- [1] Papadopoulos, I. V. (1999). Multiaxial fatigue limit criterion of metals, Dang-Van, K.; Papadopolous, I. V. (Eds.), *High-Cycle Metal Fatigue*, Springer, Vienna, 89-143, doi:[10.1007/978-3-7091-2474-1](https://doi.org/10.1007/978-3-7091-2474-1)
- [2] Milković, M.; Đonlagić, D.; Gubeljak, N. (2018). Change of residual stress due surface conditions of Al7075-T6, *Procedia Structural Integrity*, Vol. 13, 1861-1866, doi:[10.1016/j.prostr.2018.12.328](https://doi.org/10.1016/j.prostr.2018.12.328)
- [3] Dang-Van, K. (1999). Introduction to fatigue analysis in mechanical design by the multiscale approach, Dang-Van, K.; Papadopolous, I. V. (Eds.), *High-Cycle Metal Fatigue*, Springer, Vienna, 57-88, doi:[10.1007/978-3-7091-2474-1\\_2](https://doi.org/10.1007/978-3-7091-2474-1_2)

- [4] Dang-Van, K. (1993). Macro-micro approach in high-cycle multiaxial fatigue, McDowell, D. L.; Ellis, R. (Eds.), *Advances in Multiaxial Fatigue*, ASTM, Philadelphia, Vol. STP 1191, 120-130, doi:[10.1520/STP24799S](https://doi.org/10.1520/STP24799S)
- [5] Bernasconi, A.; Filippini, M.; Foletti, S.; Vaudo, D. (2006). Multiaxial fatigue of a railway wheel steel under non-proportional loading, *International Journal of Fatigue*, Vol. 28, No. 5-6, 663-672, doi:[10.1016/j.ijfatigue.2005.07.045](https://doi.org/10.1016/j.ijfatigue.2005.07.045)
- [6] Mrzyglod, M.; Zielinski, A. (2007). Multiaxial high-cycle fatigue constraints in structural optimization, *International Journal of Fatigue*, Vol. 29, No. 9-11, 1920-1926, doi:[10.1016/j.ijfatigue.2007.01.032](https://doi.org/10.1016/j.ijfatigue.2007.01.032)
- [7] Chamat, A.; Abbadi, M.; Gilgert, J.; Cochetoux, F.; Azari, Z. (2007). A new non-local criterion in high-cycle multiaxial fatigue for non-proportional loadings, *International Journal of Fatigue*, Vol. 29, No. 8, 1465-1474, doi:[10.1016/j.ijfatigue.2006.10.033](https://doi.org/10.1016/j.ijfatigue.2006.10.033)
- [8] Palin-Luc, T.; Lasserre, S. (1998). An energy based criterion for high cycle multiaxial fatigue, *European Journal of Mechanics – A/Solids*, Vol. 17, No. 2, 237-251, doi:[10.1016/S0997-7538\(98\)80084-3](https://doi.org/10.1016/S0997-7538(98)80084-3)
- [9] Flaceliere, L.; Morel, F.; Dragon, A. (2007). Competition between mesoplasticity and damage under HCF – elasticity/damage shakedown concept, *International Journal of Fatigue*, Vol. 29, No. 12, 2281-2297, doi:[10.1016/j.ijfatigue.2006.11.001](https://doi.org/10.1016/j.ijfatigue.2006.11.001)
- [10] Potter, K.; Yousefi, F.; Zenner, H. (2000). Experiences with lifetime prediction under multiaxial random loading, Kalluri, S.; Bonacuse, P. J. (Eds.), *Multiaxial Fatigue and Deformation: Testing and Prediction*, ASTM International, West Conshohocken, Vol. STP 1387, 157-172, doi:[10.1520/STP13503S](https://doi.org/10.1520/STP13503S)
- [11] Pak, Y. E. (1992). Linear electro-elastic fracture mechanics of piezoelectric materials, *International Journal of Fracture*, Vol. 54, No. 1, 79-100, doi:[10.1007/BF00040857](https://doi.org/10.1007/BF00040857)
- [12] Glišić, B.; Inaudi, D. (2010). Integrity monitoring of fracture critical bridges, *Structural Integrity and Life*, Vol. 10, No. 2, 135-141
- [13] Xia, Q.; Yao, C. Y.; Jian, Z.; Qi, Z. F. (2016). In-service condition assessment of a long-span suspension bridge using temperature-induced strain data, *Journal of Bridges Engineering*, Vol. 22, No. 3, Paper 04016124, 11 pages, doi:[10.1061/\(ASCE\)BE.1943-5592.0001003](https://doi.org/10.1061/(ASCE)BE.1943-5592.0001003)
- [14] Oh, B. K.; Park, H. S.; Glišić, B. (2021). Prediction of long term strain in concrete structure using convolutional neural networks air temperature and time stamp of measurements, *Automation in Construction*, Vol. 126, Paper 103665, 16 pages, doi:[10.1016/j.autcon.2021.103665](https://doi.org/10.1016/j.autcon.2021.103665)
- [15] Pevec, S.; Kunaver, J.; Budinski, V.; Njegovec, M.; Đonlagic, D. (2023). An all-fiber Fabry-Pérot sensor for emulsion concentration measurements, *Sensors*, Vol. 23, No. 4, Paper 1905, 13 pages, doi:[10.3390/s23041905](https://doi.org/10.3390/s23041905)
- [16] Njegovec, M.; Đonlagic, D. (2020). A fiber-optic gas sensor and method for the measurement of refractive index dispersion in NIR, *Sensors*, Vol. 20, No. 13, Paper 3717, 18 pages, doi:[10.3390/s20133717](https://doi.org/10.3390/s20133717)
- [17] Njegovec, M.; Budinski, V.; Macuh, B.; Đonlagic, D. (2022). Microbend point and distributed fiber optic corrosion sensing, *IEEE Transactions on Instrumentation and Measurement*, Vol. 71, Paper 7007112, 12 pages, doi:[10.1109/TIM.2022.3203450](https://doi.org/10.1109/TIM.2022.3203450)
- [18] Njegovec, M.; Pevec, S.; Đonlagic, D. (2021). Optical micro-wire flow-velocity sensor, *Sensors*, Vol. 21, No. 12, Paper 4025, 17 pages, doi:[10.3390/s21124025](https://doi.org/10.3390/s21124025)
- [19] Li, H.; Zhu, L.; Dong, M.; Lou, X.; Guo, Y. (2016). Analysis on strain transfer of surface-bonding FBG on Al 7075-T6 alloy host, *Optik*, Vol. 127, No. 3, 1233-1236, doi:[10.1016/j.ijleo.2015.10.227](https://doi.org/10.1016/j.ijleo.2015.10.227)
- [20] Zuñiga Tello, I. F.; Milković, M.; Dominguez Almaraz, G. M.; Gubelj, N. (2020). Ultrasonic and conventional fatigue endurance of aeronautical aluminum alloy 7075-T6, with artificial and induced pre-corrosion, *Metals*, Vol. 10, No. 8, Paper 1033, 17 pages, doi:[10.3390/met10081033](https://doi.org/10.3390/met10081033)
- [21] Burgan, H. I. (2021). Numerical modeling of structural irregularities on unsymmetrical buildings, *Technical Gazette*, Vol. 28, No. 3, 856-861, doi:[10.17559/TV-20200328103359](https://doi.org/10.17559/TV-20200328103359)
- [22] Dziubińska, A.; Surdacki, P. (2022). Numerical analysis of the new forming process of the aircraft bracket forging made of AZ91 alloy at different rates of deformation, *Technical Gazette*, Vol. 29, No. 2, 634-640, doi:[10.17559/TV-20210427084307](https://doi.org/10.17559/TV-20210427084307)

- [23] Li, W. Y.; Cheng, C. C.; Lo, Y. L. (2009). Investigation of strain transmission of surface-bonded FBGs used as strain sensors, *Sensors and Actuators A: Physical*, Vol. 149, No. 2, 201-207, doi:[10.1016/j.sna.2008.11.011](https://doi.org/10.1016/j.sna.2008.11.011)
- [24] Lamprecht, M.; Leonhartsberger, M. (2021). Tool stiffness calculation in roll forming, *International Journal of Simulation Modelling*, Vol. 20, No. 1, 40-51, doi:[10.2507/IJSIMM20-1-539](https://doi.org/10.2507/IJSIMM20-1-539)
- [25] Her, S.-C.; Huang, C.-Y. (2016). The effects of adhesive and bonding length on the strain transfer of optical fiber sensors, *Applied Sciences*, Vol. 6, No. 1, Paper 13, 9 pages, doi:[10.3390/app6010013](https://doi.org/10.3390/app6010013)
- [26] Crupi, V.; Guglielmino, E.; Maestro, M.; Marinò, A. (2009). Fatigue analysis of butt welded AH36 steel joints: thermographic method and design S-N curve, *Marine Structures*, Vol. 22, No. 3, 373-386, doi:[10.1016/j.marstruc.2009.03.001](https://doi.org/10.1016/j.marstruc.2009.03.001)
- [27] Sun, L. Q.; Jiang, K.; Zeng, Q. L.; Gao, K. D.; Zhang, X. D. (2021). Influence of drum cutting eight on shearer cutting unit vibration by co-simulation method, *International Journal of Simulation Modelling*, Vol. 20, No. 1, 111-122, doi:[10.2507/IJSIMM20-1-548](https://doi.org/10.2507/IJSIMM20-1-548)
- [28] Charkaluk, E.; Bignonnet, A.; Constantinescu, A.; Dang Van, K. (2003). Fatigue design of structures under thermomechanical loadings, *Fatigue & Fracture Engineering Materials & Structures*, Vol. 25, No. 12, 1199-1206, doi:[10.1046/j.1460-2695.2002.00612.x](https://doi.org/10.1046/j.1460-2695.2002.00612.x)
- [29] Lin, S.-J.; Quinn, S.; Matthys, D. R.; New, A. M.; Kincaid, I. M.; Boyce, B. R.; Khaja, A. A.; Rowlands, R. E. (2011). Thermoelastic determination of individual stresses in vicinity of a near-edge hole beneath a concentrated load, *Experimental Mechanics*, Vol. 51, No. 6, 797-814, doi:[10.1007/s11340-010-9379-6](https://doi.org/10.1007/s11340-010-9379-6)